Environmental Technology
Vol. 31, No. 11, October 2010, 1213–1220

Taylor & Francis
Taylor & Francis Group

In situ surface modification of molybdenum-doped organic–inorganic hybrid TiO_2 nanoparticles under hydrothermal conditions and treatment of pharmaceutical effluent

B. Shahmoradi*[a,j], I.A. Ibrahim[b], N. Sakamoto[c], S. Ananda[d], T.N. Guru Row[e], Kohei Soga[f], K. Byrappa[g], S. Parsons[h] and Yoshihisa Shimizu[i]

[a]*University of Mysore, Environmental Science Department, Karnataka 570009, India;* [b]*Central Metallurgical R&D Institute, Hellwan, Egypt;* [c]*Shizuoka University, 3-5-1 Johoku, Naka-ku, Hamamatsu-shi, Japan;* [d]*Chemistry Department, University of Mysore, Manansagangotri, Karnataka 570009, India;* [e]*Indian Institute of Science, Solid State and Structural Chemistry Unit, Bangalore 560012, India;* [f]*Department of Materials Science and Technology, Tokyo University of Science, 2641 Yamazaki, Noda, Chiba, Tokyo 278–8510, Japan;* [g]*University of Mysore, Geology Department, Karnataka 570009, India;* [h]*Cranfield University, Bedfordshire, MK43 0AL, United Kingdom;* [i]*Research Center for Environmental Quality Management, Kyoto University, 1–2 Yumihama, Otsu, Shiga 520–0811, Japan;* [j]*School of Public Health, Faculty of Environmental Health Enginnering, Kermanshah University of Medical Science, Kermanshah, Iran*

(*Received 29 September 2009; Accepted 28 December 2009*)

Molybdenum-doped TiO_2 organic–inorganic hybrid nanoparticles were synthesized under mild hydrothermal conditions by *in situ* surface modification using *n*-butylamine. This was carried out at 150°C at autogeneous pressure over 18 h. *n*-Butylamine was selected as a surfactant since it produced nanoparticles of the desired size and shape. The products were characterized using powder X-ray diffraction, Fourier transform infrared spectrometry, dynamic light-scattering spectroscopy, UV–Vis spectroscopy and transmission electron microscopy. Chemical oxygen demand was estimated in order to determine the photodegradation efficiency of the molybdenum-doped TiO_2 hybrid nanoparticles in the treatment of pharmaceutical effluents. It was found that molybdenum-doped TiO_2 hybrid nanoparticles showed higher photocatalytic efficiency than untreated TiO_2 nanoparticles.

Keywords: nanomaterials; surfactants; wastewater; solid waste management; air pollution

Introduction

In recent years TiO_2 has become recognized as a most promising photocatalytic material. A hydrothermal technique is one of the most favoured synthetic methods owing to its advantages in tailor-making TiO_2 nanoparticles of the required size, shape and properties [1–3]. Semiconductor photocatalysts have attracted great attention since they can be adapted to air, water and wastewater purification, for use in antibacterial self-cleaning materials, for dye removal, and sensors, etc. [4–7]. TiO_2 has a number of advantages, including its cost-effectiveness, high chemical stability, non-toxicity, and favourable optoelectronic properties [8]. It is for example used in dye-synthesized solar cells on the large scale due to its cost-effectiveness and ease of fabrication. Narrowing the band gap of TiO_2 is very important in order to utilize a wide range of wavelengths during photodegradation, including UV and visible light [9–11].

A number of dopants, including W, In, Nd, Mo, Mn, C, F and Cr, are employed to alter the band gap and to improve the photocatalytic activity of TiO_2 nanoparticles [12–14]. It is well known that unmodified nanoparticles have a tendency to agglomerate, and the particles are therefore not easily dispersed either in the effluent or in the treatment medium. However, addition of surface modifiers, surfactants, capping agents or organic ligands into the precursors under hydrothermal conditions can prevent agglomeration and control the size and shape of the nanoparticles. In addition the inclusion of such materials greatly alters the surface charge and can thus render the particles hydrophobic or hydrophilic as required [15–18]. With this in mind a systematic investigation of the role of surfactant on the synthesis of molybdenum-doped TiO_2 nanoparticles has been carried out with regard to their shape, size and surface charge.

*Corresponding author: Email: bshahmorady@gmail.com

ISSN 0959-3330 print/ISSN 1479-487X online

DOI: 10.1080/09593331003592261
http://www.informaworld.com

Experimental

Preparation of organic–inorganic molybdenum-doped TiO_2 hybrid nanoparticles

Molybdenum-doped TiO_2 organic–inorganic hybrid nanoparticles were synthesized under mild hydrothermal conditions (T = 150°C, P = autogeneous). Pure TiO_2 (Loba Chemie, 99% 1 M) was used as starting material and the dopant (MoO_3: 2 M%; 5 M%) was added. About 10 mL 1N HCl was added as a mineralizer. Different concentrations (0.8, 1.0, 1.2 and 1.4 M) of *n*-butylamine (Sisco Research Lab PVT, Ltd., Mumbai, India; assay (GC), 99.5%) were added to the above mixture and stirred vigorously for a few minutes. The final mixture was then transferred into a Teflon liner (V_{fill} = 50%) and placed in a general purpose autoclave held in an oven at 150°C for 18 h. The autoclave was then cooled to room temperature and the product within the Teflon liner transferred to a beaker, washed with distilled water and allowed to settle. The supernatant solution was removed by means of a syringe and the remnants centrifuged 10 min at 2000 rpm. The washing procedure was repeated three times to remove residual surfactant and solvent. The product was dried in a hot air oven at 40–50°C for a few hours. The dried particles were subjected to systematic characterization and photocatalytic study.

The resultant products were characterized using a variety of analytical techniques. The Fourier transform infrared (FTIR) spectra were recorded using an FTIR Jasco–460 Plus (Japan), at a resolution of 4 cm^{-1}. Powder X-ray diffraction (XRD) patterns were determined using a Bruker D8 Advance (Germany) at Cu Kα, λ = 1.542 Å, voltage = 40 mV, current = 30 mA and scan speed 1.5° per minute. The data were collected over the range 2θ = 5–100°. Optical properties were studied using a UV–Vis spectrophotometer (Minispec SL 171, Elico, India). The particle size and its distribution were determined by dynamic light scattering (DLS) (Horiba particle size analyzer LB–550, Japan). Transmission electron microscopy (TEM) images of the molybdenum-doped TiO_2 organic–inorganic hybrid nanoparticles were recorded using a JEM 2000FX II (JOEL Ltd., Tokyo, Japan).

Photocatalytic degradation of pharmaceutical wastewater

Pharmaceutical industrial effluents were collected and preserved according to the manual *Standard methods for the examination of water and wastewater* (American Water Works Association) [19] and treated with 2 mL H_2SO_4 per L of sample. A portion of the nanoparticles synthesized was added to a 50 mL beaker containing various concentrations of effluent collected from one of the pharmaceutical operations in the locality of Mysore City, India. The beaker and contents were isolated from air and exposed to a light source. The variables were retention time, photocatalyst concentration and type of light source in relation to the percentage of dopants in the modified molybdenum-doped TiO_2 hybrid nanoparticles synthesized. A blank sample was used as control. The intensity of sunlight and UV (8 W, Sankyo Denki, Japan) was estimated by photolysis of uranyl oxalate; the intensity of sunlight was estimated to be 6.435 × 10^{16} quanta s^{-1} and the intensity of UV as 2.375 × 10^{15} quanta s^{-1}. About 2–3 mL of the sample that had been exposed to the light was centrifuged for 4–5 min at 1500 rpm and the percent transmission (%T) measured at 540 nm using a UV–Vis spectrophotometer. The treated samples were filtered to remove photocatalysts. An assessment of chemical oxygen demand (COD) was then carried out by the open reflux method (ORM) at intervals of 30 min over 3 h.

Results and discussion

Characterization of the molybdenum-doped TiO_2 organic–inorganic hybrid nanoparticles

The results of the characterization confirm the successful synthesis of the molybdenum-doped TiO_2 hybrid nanoparticles incorporating surface modification by *n*-butylamine under mild hydrothermal conditions. The powder XRD results indicate that the nanoparticles synthesized equate well to the I41/amd space group, and also that there is a slight change in the lattice parameters of molybdenum-doped TiO_2 nanoparticles (TiO_2–X, X = 2, 5% molybdenum) by comparison with pure TiO_2. This confirms the existence of molybdenum atoms as dopant in the TiO_2 nanoparticles. The radius of the Mo(VI) ion (0.69 nm) is greater than that of Ti(IV) (0.42 nm), making the volume of the doped Mo(VI) cell larger than that of pure TiO_2.

The powder XRD pattern of (2 M%; 5 M%) molybdenum-doped TiO_2 hybrid nanoparticles shows five primary diffraction peaks, as shown in Figure 1, and these can be attributed to different diffraction planes of anatase TiO_2 [20]. The data also indicate that the cell volume of molybdenum-doped TiO_2 hybrid nanoparticles has slightly increased upon 2 M% and 5 M% molybdenum doping (Table 1) and also that there is a slight shift in the peak angles. The powder XRD data also confirm that the molybdenum is located interstitially without disturbing the basic structure of the TiO_2.

The functional groups present in the modified nanoparticles have been studied using FTIR spectroscopy. Figure 2 shows the FTIR spectra of (a) pure TiO_2, (b) undoped TiO_2 nanoparticles modified with *n*-butylamine, (c) 2 M% MoO_3-doped TiO_2 nanoparticles modified with 0.8 M *n*-butylamine, (d) 2 M% MoO_3-doped TiO_2 nanoparticles modified with 1.4 M *n*-butylamine, (e) 5 M% MoO_3-doped TiO_2 nanoparticles modified with

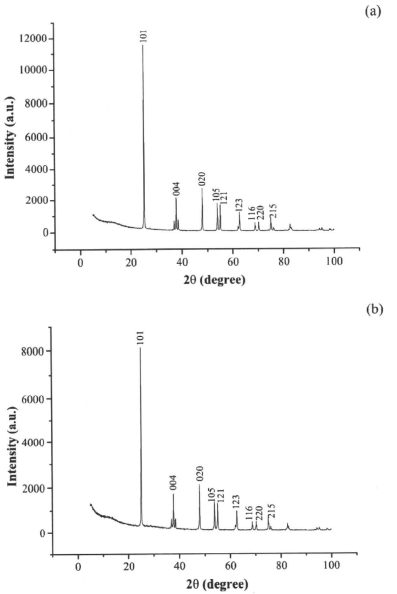

Figure 1. Powder XRD pattern of (a) 2% molybdenum-doped TiO_2; (b) 5% molybdenum-doped TiO_2 modified using 1.4 M *n*-butylamine.

Table 1. Cell dimensions of TiO_2 catalysts.

Catalyst	*a* (Å)	*c* (Å)	*a*:*c* ratio	*V* (Å^3)	Source
Pure TiO_2	3.7845	9.5143	0.3977	136.30	[24]
MoO_3 (2 M%) -doped TiO_2	3.7934	9.5456	0.3974	137.360	Present work
MoO_3 (5 M%) -doped TiO_2	3.7976	9.5732	0.3967	138.062	Present work

0.8 M *n*-butylamine, and (f) 5 M% MoO_3-doped TiO_2 nanoparticles modified with 1.4 M *n*-butylamine. As the FTIR spectra indicate, there is no hydroxyl or amine group coverage on pure TiO_2, while the modified undoped and doped TiO_2 hybrid nanoparticles show the presence of new absorption peaks, implying that the surfactant has become chemically immobilized on the surface of the undoped and Mo(VI)-doped TiO_2 nanoparticles. Moreover, the peak intensity was greater in the case of 5% molybdenum-doped TiO_2 nanoparticles compared to 2% molybdenum-doped TiO_2 hybrid nanoparticles.

It can be concluded that the molybdenum-doped TiO_2 nanoparticles synthesized with the modification indicated above have organic coverage present on their surface, and this has changed the surface properties of the nanoparticles. In the spectra of the molybdenum-doped TiO_2 hybrid nanoparticles modified with *n*-butylamine shown in Figure 2 the peak around 850 cm^{-1} exhibits a weak bond, causing stretching of the Mo–O$^-$ species of Mo–O–Ti or Mo–O$^-$ defect sites which are formed by the inclusion of Ti^{4+} ions into the MoO_3 matrices, whereas the peak around 650 cm^{-1} represents TiO_2 matrices [22]. The peaks around 1503 and 3675 cm^{-1} correspond to the presence of CH_3 and N–H stretching bonds, respectively. Similarly, the appearance of new peaks around 2965 and 3400 cm^{-1} corresponds respectively to O–H and NH_4^+ stretching bonds. The absorption peaks around 1638, 3600 and 3695 cm^{-1} are due to C=O stretching bonds.

Figure 3 shows TEM images characteristic of organic–inorganic 2% and 5% molybdenum-doped TiO_2 hybrid nanoparticles modified with 0.8 M and 1.4 M *n*-butylamine, respectively. Figure 3 demonstrates a thin organic coverage of surface modifier on the molybdenum-doped TiO_2 nanoparticles. This organic coverage was confirmed by FTIR spectra, as in Figure 2. The agglomeration was less when a higher concentration (1.4 M) of surface modifier was used. TiO_2 hybrid nanoparticles obtained with 1.0 M and 1.2 M *n*-butylamine have morphologies closer to the TiO_2 hybrid nanoparticles obtained with 0.8 M and 1.0 M *n*-butylamine, but the variation was only in respect of agglomeration and size. As the Mo(VI) concentration increased, so also did the particle size, as seen in Figure 3.

For this reason only characteristic TEM images are given in this paper. The *in situ* surface modification has led to the control of growth direction and particle size, and in preventing agglomeration. It is found that the surface modifier not only affects the dispersibility of the molybdenum-doped TiO_2 hybrid nanoparticles, but also changes their growth habit. The particle size in all cases was in the nano-range, i.e. 30–250 nm.

Figure 4 shows the particle size distribution of the molybdenum-doped TiO_2 organic–inorganic hybrid nanoparticles synthesized, confirming the nano-range of the particles. The range was narrower in the case of 5 M% molybdenum-doped TiO_2 hybrid nanoparticles.

Figure 5 shows UV–Vis absorption spectra of representative pure TiO_2 and molybdenum-doped (2 M% and 5 M%) TiO_2 nanoparticles modified with 1.0 M *n*-butylamine of different deposition modes in the 300–700 nm wavelength range. All the studies were carried out at room temperature (~25°C). Absorption started below 350 nm and there was a peak at around 380 nm for pure TiO_2 particles, but in case of the

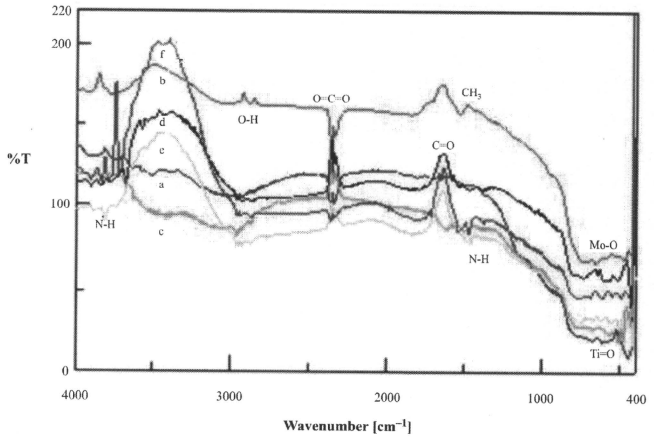

Figure 2. FTIR spectra of (a) pure TiO_2, (b) undoped TiO_2 nanoparticles modified with 0.5 M *n*-butylamine, (c) 2 M% MoO_3-doped TiO_2 nanoparticles modified with 0.8 M *n*-butylamine (d) 2 M% MoO_3-doped TiO_2 nanoparticles modified with 1.4 M *n*-butylamine, (e) 5 M% MoO_3-doped TiO_2 nanoparticles modified with 0.8 M *n*-butylamine, and (f) 5 M% MoO_3-doped TiO_2 nanoparticles modified with 1.4 M *n*-butylamine.

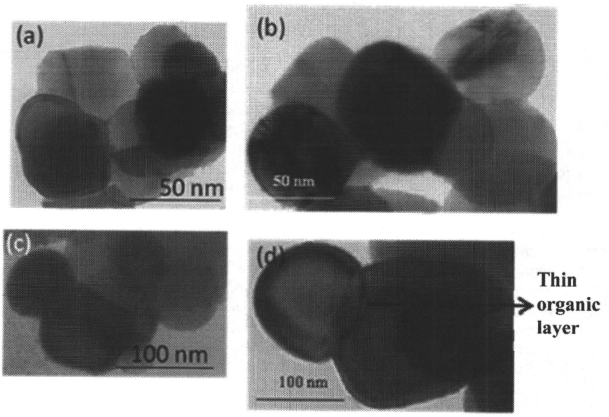

Figure 3. TEM image of molybdenum-doped TiO_2 hybrid nanoparticles: (a) 2 M% molybdenum, 0.8 M *n*-butylamine; (b) 2 M% molybdenum, 1.4 M *n*-butylamine, (c) 5 M% molybdenum, 0.8 M *n*-butylamine, and (d) 5 M% molybdenum,1.4 M *n*-butylamine.

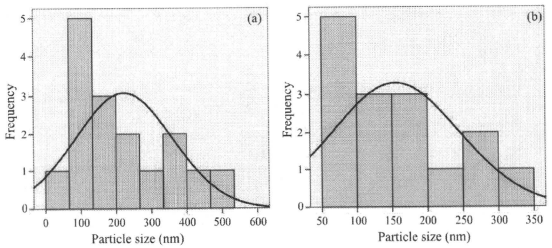

Figure 4. Particle size distribution using DLS for (a) 2 M% molybdenum-doped; (b) 5 M% molybdenum-doped TiO_2 hybrid nanoparticles modified using 1.4 M *n*-butylamine.

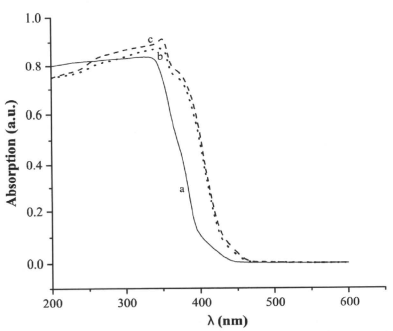

Figure 5. UV–Vis absorbance spectra of (a) pure TiO_2, (b) surface-modified 2% molybdenum-doped TiO_2 nanoparticles, and (c) surface-modified 5% molybdenum-doped TiO_2 nanoparticles.

modified Mo-doped TiO_2 hybrid nanoparticles the absorption extended into the visible region, starting at around 450 nm. The absorption edge of TiO_2 in surface-modified Mo-doped TiO_2 hybrid nanoparticles observed above 390 nm indicates a significant *blue shift* of band gap energy comparable to pure TiO_2, which confirms the substitution of dopant in the TiO_2 nanoparticle structure [23]. It follows that the photodegradation efficiency can be significantly increased in the visible region in a way which cannot be achieved in the case of pure TiO_2. Suitable doping would therefore be of benefit in TiO_2 photocatalysis in conditions of visible or sunlight. Moreover, tailoring the morphology of TiO_2 nanoparticles synthesized through doping and surface modification results in rounded nanoparticles, which are more effective than facetted nanoparticles of pure TiO_2 in photocatalytic applications owing to their larger surface area [24].

Photocatalytic treatment studies

The photocatalytic activity of pure TiO_2, and molybdenum-doped TiO_2 nanoparticles with and without surface modifier, were studied using pharmaceutical effluent containing a variety of organic compounds. The retention time was up to 3 h and concentration of photocatalyst was varied to determine the optimum quantity required to achieve the highest photocatalytic efficiency. Figure 6 shows that molybdenum-doped TiO_2 nanoparticles exhibited much greater activity than pure TiO_2 or molybdenum-doped TiO_2 without modifier in the visible region under UV and sunlight, respectively. The best result for COD reduction was achieved at 1.6 g L^{-1} of 5% modified molybdenum-doped TiO_2 nanoparticles under sunlight and after 3 h contact time, resulting in 93% degradation of the pharmaceutical effluent.

Figure 7 shows %*T* of the photodegraded pharmaceutical effluent sample using modified 5 M% molybdenum-doped TiO_2 nanoparticles (1.6 g L^{-1}) under UV and sunlight, respectively. Molybdenum doping leads to the partial reduction of Ti^{4+} to Ti^{3+}, which can be expected to improve the photocatalytic activity of TiO_2 since Ti^{3+} sites could act as photogenerated electron traps and thus facilitate charge separation [25].

Addition of surfactant causes the molybdenum-doped TiO_2 nanoparticles to grow preferentially in certain directions and gives rounded, equidimensional nanoparticles. These are more effective since they absorb a greater degree of light, improving their photodegradation efficiency compared with molybdenum-doped TiO_2 particles synthesized without modifier. Nevertheless, it should be borne in mind that although the addition of surfactant is one of the best techniques for tailoring the morphology and reducing particle size,

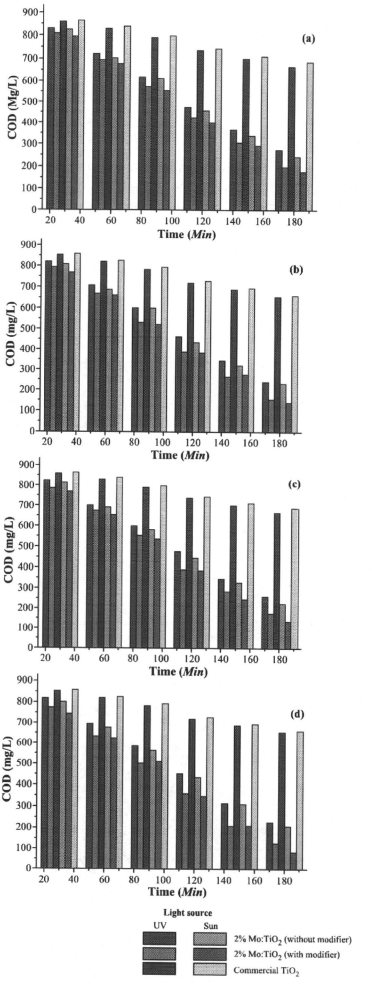

Figure 6. Effect of light source (UV or sun light) and catalyst type (reagent grade TiO_2, unmodified 2 M% Mo:TiO_2 and modified 2M% Mo:TiO_2 nanoparticles) vs. detention time on COD reduction efficiency of pharmaceutical wastewater: (a) 1.2 g L^{-1} catalyst; (b) 1.6 g L^{-1} catalyst (dopant = 5%); (c) 1.2 g L^{-1} catalyst; (d) 1.6 g L^{-1} catalyst (dopant = 2%).

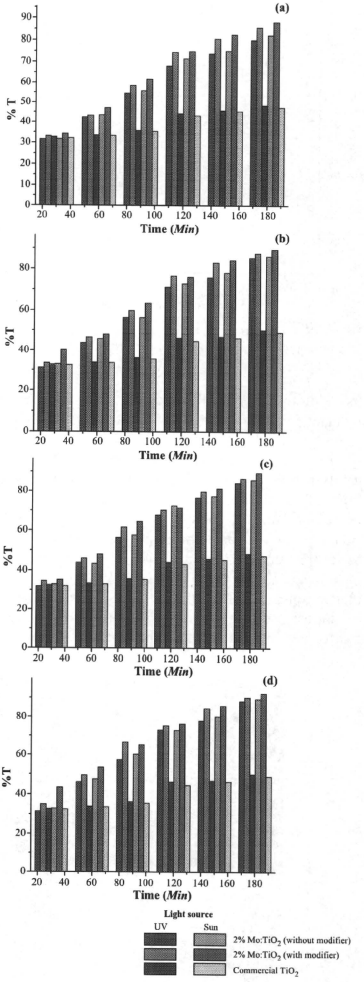

Figure 7. Effect of light source (UV or sun light) and catalyst type (reagent grade TiO_2, unmodified 2 M% Mo:TiO_2 and modified 2M% Mo:TiO_2 nanoparticles) vs. detention time on %T efficiency of pharmaceutical wastewater: (a) 1.2 g L^{-1} catalyst; (b) 1.6 g L^{-1} catalyst (dopant = 5%); (c) 1.2 g L^{-1} catalyst; (d) 1.6 g L^{-1} catalyst (dopant = 2%).

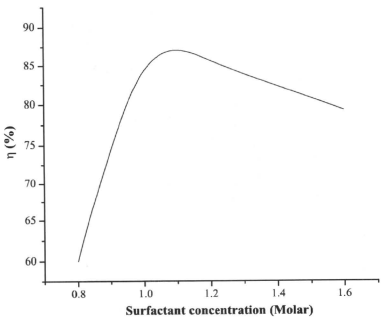

Figure 8. Relationship between concentration of *n*-butylamine and photodegradation efficiency (η).

its addition beyond the optimal concentration will reduce the photodegradation efficiency, as illustrated in Figure 8.

The optimum concentration of surfactant for photocatalytic efficiency was found to be 1.0 M. The proportion of surfactant used should be less than the precursors and the solvent to give effective modification. Surfactant at the appropriate concentration is likely to form a very thin organic layer around the nanoparticles, which allows the main properties of the nanoparticles to remain unaltered.

Figure 9 illustrates the highly monodispersed and hydrophilic behaviour of the nanoparticles synthesized using *n*-butylamine as surfactant. The hydrothermal technique has advantages in the presence of surfactants in obtaining highly efficient hybrid nanoparticles with wide a range of potential application.

Conclusions

Organic–inorganic molybdenum-doped TiO_2 hybrid nanoparticles modified *in situ* using *n*-butylamine under mild hydrothermal conditions have been successfully synthesized. The resultant products were in the nanosize range and the results clearly revealed the effect of the *in situ* modification in terms of particle size and morphology. Molybdenum doping of the nanoparticles leads to a shift in photoabsorption into the visible light region.

The results of the photodegradation of pharmaceutical effluent containing high concentrations of various complex organic compounds demonstrate the promise of these nanoparticles in the effective treatment of such industrial effluents. Doping with a suitable molar percentage of metal oxide enhances photodegradation due to a significant blue shift of band gap energy into the visible light region.

The use of modifiers can increase the surface area to volume ratio by stunting the growth of larger particles and preventing agglomeration. This takes advantage of the fact that smaller particles are more effective as photocatalysts. The amount of surfactant has a significant effect on the morphology and size of the particles. The results achieved with 1.0 M *n*-butylamine are seen to be highly encouraging for the photodegradation of industrial effluents.

Figure 9. Hydrophilic and high dispersiblity effect of *in situ* modification of TiO_2 nanoparticles with *n*-butylamine.

References

[1] K. Tomita, M. Kobayashi, V. Petrykin, S. Yin, T. Sato, M. Yoshimura, and M. Kakihana, *Hydrothermal synthesis of TiO_2 nano-particles using novel water-soluble titanium complexes,* J. Mater. Sci. 43 (2005), pp. 2217–2221.

[2] Y. Hakuta, H. Hayashi, and K. Arai, *Preparation of metal oxide nanowires by hydrothermal synthesis in supercritical water,* Mater. Res. Soc., Symposium Proceedings, 2004, p. 789.

[3] F. Sayilkan, M. Asilturk, S. Sener, S. Erdemoglu, M. Erdemoglu, and H. Syilkan, *Hydrothermal synthesis, characterization and photocatalytic activity of nano-sized TiO_2 based catalysts for Rhodamine B degradation,* Turkish J. Chem. 31 (2007), pp. 211–221.

[4] I. Oller, W. Gernjak, M.I. Maldonado, L.A. Pérez-Estrada, J.A. Sánchez-Pérez, and S. Malato, *Solar photocatalytic degradation of some hazardous water-soluble pesticides at pilot-plant scale,* J. Hazard. Mater. 138 (2006), pp. 507–517.

[5] R. Bellobono, F. Morazzoni, and P. Tozzi, *Photocatalytic membrane modules for drinking water purification in domestic and community appliances,* Internat. J. Photoenergy 07 (2005), pp. 109–113.

[6] K. Byrappa, A.K. Subramani, S. Ananda, K.M. Lokanatha Rai, and R. Dinesh, *Photocatalytic degradation of Rhodamine B dye using hydrothermally synthesized ZnO,* Bull. Mater. Sci. 29 (2006), pp. 433–438.

[7] N. Savage and S. Mamadou Diallo, *Nanomaterials and water purification: Opportunities and challenges,* J. Nanoparticle Res. 7 (2005), pp. 331–342.

[8] A. Sobczyński and A. Dobosz, *Water purification by photocatalysis,* Pol. J. Environ. Stud. 10 (2001), pp. 195–205.

[9] D. Belapurkar, P. Sherkhane, and S.P. Kale, *Disinfection of drinking water using photocatalytic techniques,* Curr. Sci. 91 (2006), pp. 73–76.

[10] Y. Wang, H. Cheng, Y. Hao, J. Ma, W. Li, and S. Cai, *Preparation, characterization and photoelectrochemical behaviors of Fe(III)-doped TiO_2 nanoparticles,* J. Mater. Sci. 34 (1999), pp. 3721–3729.

[11] Q. Wang, Zh. Jiang, Y. Wang, D. Chen, and D. Yang *Photocatalytic properties of porous C-doped TiO_2 and Ag/C-doped TiO_2 nanomaterials by eggshell membrane templating,* J. Nanoparticle Res. 11 (2009), pp. 375–384.

[12] S. Zhang, Y. Chen, Y. Yu, H. Wu, S. Wang, B. Zhu, W. Huang, and S. Wu, *Synthesis, characterization of Cr-doped TiO_2 nanotubes with high photocatalytic activity,* J. Nanoparticle Res. 10 (2008), pp. 871–875.

[13] S. Lee, C.Y. Yun, M.S. Hahn, J. Lee, and J.H. Yi, *Synthesis and characterization of carbon-doped titania as a visible-light-sensitive photocatalyst,* Korean J. Chem. Eng. 25 (2008), pp. 892–896.

[14] Y. Yu, H.-H. Wu, B. Zhu, S. Wang, W. Huang, S. Wu, and Sh. Zhang, *Preparation, characterization and photocatalytic activities of F-doped TiO_2 nanotubes,* Catal. Lett. 125 (2008), pp. 165–171.

[15] K. Dhermendra Tiwari, J. Behari and P. Sen, *Application of nanoparticles in waste water treatment,* World App. Sci. J. 3 (2008), pp. 417–433.

[16] N. Kometani, A. Fujita, and Y. Yonezawa, *Synthesis of N-doped titanium oxide by hydrothermal treatment,* J. Mater. Sci. 43 (2008), pp. 2492–2498.

[17] S.Y. Kuo, W.C. Chen, F.I. Lai, C.P. Cheng, H.C. Kuo, S.C. Wang, and W.F. Hsieh, *Effects of doping concentration and annealing temperature on properties of highly-oriented Al-doped ZnO films,* J. Cryst. Growth 287 (2006), pp. 78–84.

[18] T. Adschiri and K. Byrappa, *Supercritical hydrothermal synthesis of organic–inorganic hybrid nanoparticles: Nano-hybridization of organic–inorganic materials,* A. Muramatsu, ed., Birkhäuser, Germany: Springer-Verlag, 2008, pp. 217–250.

[19] S. Lenore Clescerl, A.E. Greenberg, and A.D. Eaton, *Standard Methods for Examination of Water and Wastewater,* 21st ed., American Water Works Association, 2005.

[20] N. Shahina Begum, H.M. Farveez Ahmad, and O.M. Hussain, *Characterization and photocatalytic activity of boron-doped TiO_2 thin films prepared by liquid phase deposition technique,* Bull. Mater. Sci. 31 (2008), pp. 741–745.

[21] C.J. Howard, T.M. Sabine, and F. Dickson *Structural and thermal parameters for rutile and anatase,* Acta Crystallogr. 47 (1992), pp. 462–468.

[22] M.A. Behnajady, N. Modirshahla, M. Shokri, H. Elham, and A. Zeininezhad, *The effect of particle size and crystal structure of titanium dioxide nanoparticles on the photocatalytic properties,* J. Environ. Sci. Health, Part A 43 (2008), pp. 460–467.

[23] S.S. Srinivasan, J. Wade, and E.K. Stefanakos, *Visible light photocatalysis via CdS/TiO_2 nanocomposite materials,* J. Nanomaterials 1 (2006), pp. 1–7.

[24] A.K. Subramani, K. Byrappa, G.N. Kumaraswamy, H.B. Ravishankar, C. Raganathaiah, K.M.I. Rai, S. Ananda, and M. Yashimura, *Hydrothermal preparation and characterization of Ti–AC composites,* Mater. Lett. 61 (2007), pp. 4828–4831.

[25] B.J. Saikia, G. Parthasarathy, and N.C. Sarmah, *Fourier transform infrared spectroscopic estimation of crystallinity in SiO_2 based rocks,* Bull. Mater. Sci. 31 (2008), pp. 775–779.

DOI: 10.1002/ejic.201000201

NIR Bioimaging: Development of Liposome-Encapsulated, Rare-Earth-Doped Y_2O_3 Nanoparticles as Fluorescent Probes

Kohei Soga,*[a,b,c] Kimikazu Tokuzen,[a] Kosuke Tsuji,[a] Tomoyoshi Yamano,[d] Hiroshi Hyodo,[a,b,c] and Hidehiro Kishimoto[c,d]

Keywords: Bioimaging / Rare earths / Liposomes / Ceramics / Fluorescent probes / Nanoparticles

Near-infrared (NIR) bioimaging is attracting a lot of attention due to the absence of strong scattering and color fading of the phosphors, which can provide long-term and deep imaging. For fluorescence bioimaging (FBI) in the NIR region, rare-earth-doped ceramic nanoparticles can be one of the best candidates. For the delivery of the ceramic particles to the biological imaging target, liposome-encapsulating the ceramic phosphor is proposed. Liposome-encapsulated, Er-doped Y_2O_3 nanoparticles were prepared as fluorescent probes for NIR bioimaging. Their surface was modified with PEG, biotin, anionic, and cationic agents. The dispersion, surface charge, and specific interactions of the surface-modified liposomes were characterized. Microscopic and macroscopic NIR bioimages were demonstrated by injecting the liposome-encapsulated, Er-doped Y_2O_3 nanoparticles into the body of a mouse through the blood vessels. The NIR fluorescence images of the mouse organs are presented.

Introduction

Fluorescence bioimaging (FBI) is one of the most important methods for biological research and medical diagnosis to visualize the spatial distribution and transient movement of substances in biological systems as multicolor images. Currently, major problems of FBI are shallow observation depth due to scattering, color fading of the organic phosphors, autofluorescence that causes background noise, and damage to the biological objects, which are mostly caused by the irradiation of short-wavelength excitation light, such as UV or blue light, to obtain visible fluorescence.[1] On the other hand, the fluorescence may not be "visible" to the naked eye, as most bioimaging procedures are carried out by using charge-coupled device (CCD) cameras. Therefore, the FBI in the near-infrared (NIR) is attracting interests in the fields of biological and medical research. The NIR wavelength region between 800 and 1700 nm is known as a "biological window" where one can expect the lowest loss of light due to scattering.[2] The region does not suffer from IR absorption due to molecular vibration. Because of the low quantum energy of the photon in this region, the light to be used for excitation is not harmful to biological subjects and fluorescent phosphors.

As materials that can emit fluorescence in the NIR region, rare-earth-doped ceramics have been applied as laser or optical amplifier media for decades. 1064 nm emission under 800 nm excitation from Nd:YAG is used for one of the most popular solid-state lasers.[3] 1550 nm emission under 980 nm excitation from Er^{3+}-doped silicate glass fiber is used for optical amplifiers in optical communication.[4] Those applications originate from the characteristic electronic states of 4f electrons, narrow-energy bands, and weak electron–phonon coupling, as results of the shielding effect by the outer-lying filled 5s and 5p shells. Some of the rare-earth-doped ceramics are known to show upconversion (UC) emission, which is an infrared-to-visible conversion through stepwise excitation among the discrete energy levels of the rare-earth ions in ceramics.[1] The use of this phenomenon for bioimaging has been proposed since 1999.[5–11] Our group has also worked on UC FBI in the recent years, focusing on the development of imaging probe materials.[1,12–18]

In recent years, we have been developing NIR-NIR bioimaging systems by using the NIR fluorescence at 1550 nm under 980 nm excitation, which can be efficiently emitted from Er-doped yttrium oxide (Y_2O_3:Er^{3+}) phosphors, as shown in Figure 1.[19] The development of the imaging system now allows the application of InGaAs-CCD, which can detect the light in the NIR wavelength region.

[a] Department of Materials Science and Technology, Tokyo University of Science,
2641 Yamazaki, Noda, Chiba 278-8510, Japan
Fax: +81-4-7124-1526
E-mail: mail@ksoga.com
[b] Polyscale Technology Research Center (PTRC), Tokyo University of Science,
2641 Yamazaki, Noda, Chiba 278-8510, Japan
[c] Center for Technologies against Cancer (CTC), Tokyo University of Science,
2669 Yamazaki, 278-0022 Chiba, Japan
[d] Research Institute for Biological Sciences, Tokyo University of Science,
2669 Yamazaki, 278-0022 Chiba, Japan

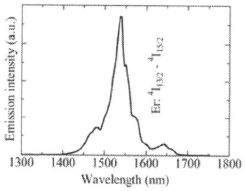

Figure 1. Emission spectrum of Er-doped Y_2O_3 nanoparticles in the NIR region.[19]

To use the Y_2O_3:Er^{3+} nanoparticles for NIR bioimaging, it is required to deliver the particles to the targeted part of the biological system. Liposome is a good candidate as a material with a similar structure as the cell membrane, and the use of liposome has been attracting interest in the research field of drug delivery. In the present study, liposome-encapsulated Y_2O_3:Er^{3+} nanoparticles with various surface properties were prepared. The obtained liposomes were tested by using an NIR fluorescence plate assay. As a demonstration of NIR-NIR bioimaging, the distribution of the liposomes injected through the blood vessels into the body of a mouse was also observed by using microscopic and macroscopic NIR FBI systems.

Results and Discussion

The encapsulation of the Y_2O_3:Er^{3+} nanoparticles were checked by observation by FE-SEM. Figure 2 shows the FE-SEM images of the liposome encapsulation of the particles under different accelerating voltages. Figure 2(a) shows the image under smaller voltage, where the outlines of the liposomes were observed. In Figure 2(b), under higher voltage, the Y_2O_3:Er^{3+} nanoparticles were observed through the liposome skin layer. From those images, we conclude that the Y_2O_3:Er^{3+} nanoparticles were encapsulated in the liposome. The average size of the Y_2O_3:Er^{3+} nanoparticles were approximately 150 nm, which matches the size estimated by dynamic light scattering (DLS) before the encapsulation. We have previously reported that particle size estimations by SEM, TEM, and DLS match.[17] The size of the liposomes dried in vacuo and observed under a microscope were approximately 500 nm.

Figure 3 shows the fluorescence images of the liposome-encapsulated Y_2O_3:Er^{3+} nanoparticles under an optical microscope. The bright-field image [Figure 3(a)] shows that the size of the wet liposome is approximately 650 nm. Figure 3(b, c) shows the upconversion fluorescence image,[1] which can be observed with a CCD camera for visible light under 980 nm NIR excitation. Figure 3(d) shows the NIR fluorescence image at 1550 nm, which was observed by an NIR CCD camera. The difference between the scales of a–c and d is due to the difference in the resolution of the used CCD cameras. All of the pictures show that the liposome is filled with Y_2O_3:Er^{3+} nanoparticles.

Figure 2. FE-SEM images of liposome-encapsulated Y_2O_3:Er^{3+} nanoparticles. Accelerating voltages are (a) 1 kV and (b) 10 kV.

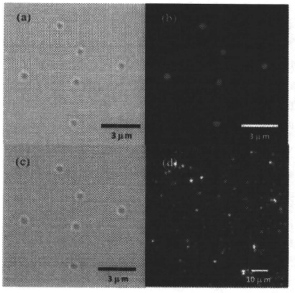

Figure 3. Fluorescence microscope images of liposome-encapsulated Y_2O_3:Er^{3+} nanoparticles. Imaging schemes are (a) bright-field image, (b) UC fluorescence image, (c) (a) + (b) and (d) NIR fluorescence image.

Because of the use of dipalmitoyl phosphatidylglycerol (DPPG), the surface of the liposome should be negatively charged. Figure 4 shows the ζ potentials of the bare and liposome-encapsulated Y_2O_3 particles. It is known that Y_2O_3 is positively charged under neutral conditions,[15] as shown in the figure. In contrast to semiconductor or metal particles, ceramic nanoparticles are normally insulators, and their surface charge cannot be determined by the type of electric carrier. Y_2O_3 comprises ionic bonding. The positive charge may be caused by the higher positive charge of Y^{3+} relative to that of O^{2-}, which causes higher localized positive charge. On the other hand, the liposome-encapsulated Y_2O_3 shows strong negative charge, which implies that the surface of the liposome consists of negatively charged DPPG.

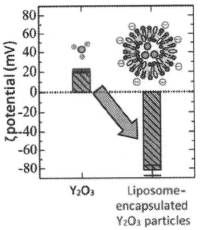

Figure 4. ζ potential of Y_2O_3 particles and liposome-encapsulated Y_2O_3 particles at pH 7.0.

Ceramic nanoparticles are normally dispersed in pure water because of the surface charge of the ceramics. However, under physiological conditions with strong ionic character, the charge is cancelled, and they agglomerate quickly to decrease the large specific energy. Figure 5 shows the transient change in the transmittance of the suspension of the bare and liposome-encapsulated Y_2O_3 nanoparticles measured at 550 nm. In case of the bare Y_2O_3 nanoparticles, the transmittance quickly decreases because of the sedimentation of the particles due to agglomeration. On the other hand, in the case of the liposome-encapsulated particles, it slowly decreases. The encapsulation of the particles by the liposome is shown to enhance the dispersion stability of the Y_2O_3 nanoparticles as bioimaging fluorescence probes.

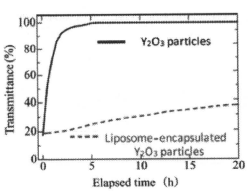

Figure 5. Sedimentation behavior of bare and liposome-encapsulated Y_2O_3 particles in a physiological saline solution (150 mM $NaCl_{aq}$, with pH 7.0).

Important characteristics of fluorescent probes to be used as bioimaging probes are dispersion stability under physiological conditions, the absence of nonspecific interaction with nontargeted substances, and specific interaction with the targeted objects. The first requirement is present in the liposome-encapsulated Y_2O_3 nanoparticles, as shown in Figure 5. Specific interaction with the targeting object was achieved by introducing PEG and biotin in the liposome skin layer. PEG is known to avoid nonspecific interaction with subjects for the use of materials with biological functions.[13–15,20–33] Biotin is a molecule known to specifically interact only with avidin in the biological system. By using streptavidin, biotinylated agents can be specifically combined to other biotinylated ligands to deliver the agents to a target. In this work, PEG and biotin were introduced to the surface of the liposome by using PEG-distearoylglycerol (PEG-DSG) and dipalmitoyl phosphoethanolamine-*N*-biotinylsodium salt (DPPE-biotin). Upon the introduction of the PEG-DSG and/or DPPE-biotin, there was no obvious change in the SEM and optical microscope observation. Figure 6 shows the results of the fluorescence plate assay by the fluorescence of the $Y_2O_3:Er^{3+}$ nanoparticles at 1550 nm under 980 nm excitation. The tested plates are with streptavidin as a target agent and bovine serum albumin (BSA) as a nontarget protein.

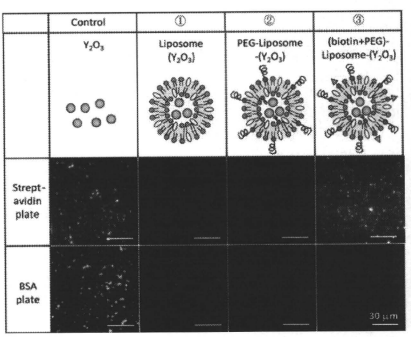

Figure 6. Evaluation of specific interaction of liposome-encapsulated $Y_2O_3:Er^{3+}$ nanoparticles by fluorescence plate assay on streptavidin and BSA plates. Bare and liposome-encapsulated $Y_2O_3:Er^{3+}$ nanoparticles are compared to those in which the liposome was modified with PEG and with PEG and biotin.

The bare $Y_2O_3:Er^{3+}$ nanoparticles interacted with both plates. The $Y_2O_3:Er^{3+}$ particles encapsulated in the liposome interacted much less than the bare particles, though still some particles were observed on both plates. The $Y_2O_3:Er^{3+}$ nanoparticles encapsulated in PEGylated liposomes were not observed in any of the plates. This result shows that the PEGylation certainly avoids the nonspecific interaction of the liposome-encapsulated $Y_2O_3:Er^{3+}$ nanoparticles with proteins. By introducing biotin into the PEGylated liposome, the $Y_2O_3:Er^{3+}$ nanoparticles can only be observed on the surface of the streptavidin plate and not on the BSA plate. As a result, liposome-encapsulated $Y_2O_3:Er^{3+}$ nanoparticles with both PEGylation and biotin modification are useful as a probe for NIR biological imaging.

As a demonstration of the use of the liposome-encapsulated $Y_2O_3:Er^{3+}$ nanoparticles as bioimaging probes, the liposomes were injected into a mouse and its organs were observed by using macroscopic and microscopic NIR FBI systems. The surfaces of the liposomes were controlled to be anionic, cationic, and PEGylated by using DPPG, stearylamine, and PEG-DSG, respectively. Figure 7 shows the NIR fluorescence images at 1550 nm under 980 nm excitation. The injected suspension was HEPES buffer (2 mL,

20 mM) with NaCl (150 mM) dispersed with Y_2O_3:Er^{3+} particles (5 mg/mL). For the following cases, a certain amount of Yb^{3+} was co-doped into Y_2O_3:Er^{3+} as a fluorescence sensitizer. The mouse skin was opened for clear observation. In all cases, the fluorescence of the Y_2O_3:Er^{3+} nanoparticles was observed from the liver. The results show that the lipofected Y_2O_3:Er^{3+} nanoparticles tend to concentrate in the liver when injected into the blood vessel via the tail vain.

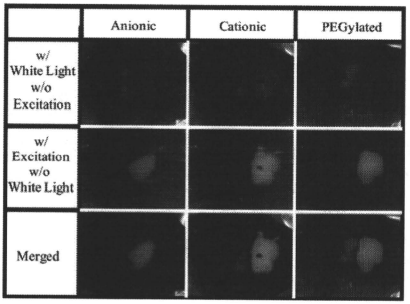

Figure 7. NIR fluorescence images of mouse organs injected with anionic, cationic, and PEGylated liposome-encapsulated Y_2O_3:Er^{3+} nanoparticles. The brightly illuminated organ is the liver.

Figure 8 shows the NIR fluorescence microscopic images of the sections from various organs of the same mouse as above. Certain amounts of the particles were found in both the liver and the spleen. No particles were found in the kidney. The difference due to the PEGylation was found in the spleen. Liposome particles with anionic and cationic surface were found both in the liver and in the spleen, while those with PEGylation were not found in the spleen. Studies to clarify the biological and medical meaning of this distribution of the probes are now in progress.

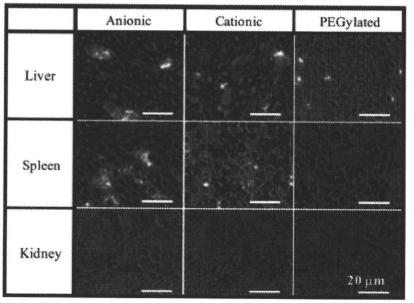

Figure 8. NIR fluorescence microscopic images of histological sections of various organs of a mouse injected with anionic, cationic, and PEGylated liposome-encapsulated Y_2O_3:Er^{3+} nanoparticles.

Conclusions

Liposome-encapsulated, Er-doped Y_2O_3 nanoparticles with various surface modifications as a fluorescent probe for NIR bioimaging were successfully fabricated. By introducing PEG on the surface of the liposome, nonspecific interaction with a protein was avoided. The liposome whose surface was modified with both biotin and PEG specifically interacted with streptavidin. Organs of a mouse injected with the liposome were imaged by both microscopic and macroscopic NIR imaging systems as a demonstration of NIR bioimaging.

Experimental Section

The preparation of Y_2O_3:Er^{3+} nanoparticles is described precisely elsewhere.[13–17] The particles were obtained by calcination of the precursor precipitated by using homogeneous precipitation. The obtained particles can emit 550 and 660 nm visible light through the upconversion process and 1550 nm light through the normal fluorescence process under 980 nm excitation by a laser diode.

Liposome-encapsulated Y_2O_3:Er^{3+} nanoparticles were prepared by the complex emulsion method.[34] HEPES buffer (2 mL, 10 mmol/L, pH 7.4 with 150 mmol/L NaCl) dispersed with PEG-modified Y_2O_3:Er^{3+} particles[14] (5 mg/mL) was added to phospholipid solution (4 mL) to form a water-in-oil (W/O) emulsion. The phospholipid solution was a chloroform solution with dipalmitoyl phosphatidylcholine (DPPC), DPPG, and cholesterol. The concentration was adjusted so that the total lipid concentration would be 30 μmol/L. The W/O emulsion was then moved to HEPES buffer solution (200 mL, 20 mmol/L, pH 7.4 with 150 mmol/L NaCl) with DPPC to form a water-in-oil-in-water (W/O/W) emulsion. The solution was stirred during the mixing and after the mixing for 12 h in a fume hood to evaporate the chloroform at room temperature. The absence of cloroform was checked by smelling the solution. DS-PEG and DPPE-biotin were added to the buffer solution at the last stage for the introduction of the PEG and biotin. The obtained liposome-encapsulated Y_2O_3:Er^{3+} nanoparticles were centrifugally washed two times with HEPES buffer solution (200 mL, 20 mmol/L, pH 7.4 with 150 mmol/L NaCl). The liposome-encapsulated Y_2O_3:Er^{3+} nanoparticles were finally dispersed in the same buffer solution such that the Y_2O_3:Er^{3+} concentration was 5 mg/mL.

The liposome solutions injected to the mouse were prepared by the method described above with the compositions listed in Table 1.

Table 1. Percent composition of the solution of the liposome injected to the mouse [mol-%].

Liposome	DPPC	Cholesterol	Additive	Amount
Anionic	40	40	DPPG	20
Cationic	40	40	stearylamine	20
PEGylated	50	40	PEG-DSG	10

The samples were injected into the blood vessel of a mouse via the tail vain. The mouse was kept alive in a cage for two hours and moved for organ imaging. The mouse was sacrificed for histology 20 min after the organ imaging. For the histological observation, the organs of the mouse were dissected, embedded in Tissue-Tek (Sacura), and snap frozen in liquid nitrogen. 7 μm cryosections were fixed in acetone at –20 °C and air-dried for 30 min. The section was stained with hematoxylin–eosin (HE) and subjected to the microscopic observation shown in Figure 8.

The NIR microscopic bioimaging system is equipped with a NIR CCD (InGaAs-CCD), as well as a laser diode at 980 nm. The optical components, such as the lens, mirror, and filters are designed so that one can observe an image with 1550 nm emission under 980 nm excitation.

The NIR macroscopic bioimaging system, so-called in vivo imaging system (IVIS), consists of a 980 nm fiber-pigtailed diode laser, a laser scanner, and a NIR (InGaAs) CCD camera, which can capture images in the 800–1700 nm wavelength region.

Acknowledgments

The authors thank to Prof. Y. Nagasaki of the University of Tsukuba and his group member for advisories on experiments. This work was supported by "Academic Frontier" Project for Private Universities: Matching Fund Subsidy from MEXT (Ministry of Education, Culture, Sports, Science and Technology), 2006-2010/2009-2013.

[1] K. Soga, *Application of Ceramic Nanophosphors for Biomedical Photonics* (Ed.: M. C. Tan), Transworld Research Network, Kerala, India, **2009**, pp. 223–241.
[2] R. R. Anderson, J. A. Parrash, *J. Invest. Dermatol.* **1981**, *77*, 13–19.
[3] R. C. Powell, *Physics of Solid State Laser Materials*, Springer, New York, NY, **1998**.
[4] S. Sudo (Ed.), *Optical Fiber Amplifiers: Materials, Devices, and Applications*, Artech House Publishers, Norwood, MA, **1997**.
[5] H. J. M. A. A. Jijlmans, J. Bonnet, J. Burton, K. Kardos, T. Vail, R. S. Niebala, H. J. Tanke, *Anal. Biochem.* **1999**, *267*, 30–36.
[6] P. Corstjens, M. Zuiderwijk, A. Brink, S. Li, H. Feindt, R. S. Neidbala, H. Tanke, *Clin. Chem.* **2001**, *47*, 1885.
[7] F. van de Rijke, H. Zijlmans, S. Li, T. Vail, A. K. Raap, R. S. Niedbala, H. J. Tanke, *Nat. Biotechnol.* **2001**, *19*, 273–276.
[8] J. Hampl, M. Hall, N. A. Mufti, Y. M. M. Yao, D. B. MacQueen, W. H. Wright, D. E. Cooper, *Anal. Biochem.* **2001**, *288*, 176–187.
[9] R. S. Niedbala, H. Feindt, K. Kardos, T. Vail, J. Burton, B. Bielska, S. Li, D. Milunic, P. Bourdelle, R. Vallejo, *Anal. Biochem.* **2001**, *293*, 22–30.
[10] K. Kuningas, T. Ukonaho, H. Pakkila, T. Rantanen, J. Rosenberg, T. Lovgren, T. Soukka, *Anal. Chem.* **2006**,*76*, 4690–4696.
[11] C. G. Morgan, A. C. Mitchell, *Biosens. Bioelectron.* **2007**, *22*, 1769–1775.
[12] K. Soga, T. Tsuji, F. Tashiro, J. Chiba, M. Oishi, K. Yoshimoto, Y. Nagasaki, K. Kitano, S. Hamaguchi, *J. Phys., Conf. Ser.* **2008**, *106*, 012023–1–5.
[13] Y. Saito, K. Shimizu, M. Kamimura, H. Furusho, K. Soga, Y. Nagasaki, *Trans. Mater. Res. Soc. Jpn.* **2008**, *33*, 803–806.
[14] K. Soga, R. Koizumi, M. Yamada, D. Matsuura, Y. Nagasaki, *J. Photopolym. Sci. Technol.* **2005**, *18*, 73–74.
[15] M. Kamimura, D. Miyamoto, Y. Saito, K. Soga, Y. Nagasaki, *Langmuir* **2008**, *24*, 8864–8870.
[16] T. Zako, H. Nagata, N. Terada, M. Sakono, K. Soga, M. Maeda, *J. Mater. Sci.* **2008**, *45*, 5325–5330.
[17] N. Venkatachalam, Y. Saito, K. Soga, *J. Am. Ceram. Soc.* **2009**, *92*, 1006–1010.
[18] T. Zako, H. Nagata, N. Terada, A. Utsumi, M. Sakono, M. Yohda, H. Ueda, K. Soga, M. Maeda, *Biochem. Biophys. Res. Commun.* **2009**, *381*, 54–58.
[19] K. Soga, K. Tokuzen, K. Tsuji, T. Yamano, N. Venkatachalam, H. Hyodo, H. Kishimoto, *Proc. SPIE* **2010**, *7598*, 759807 (9 pp.).
[20] S. Sivakumar, P. R. Diamente, F. C. van Veggel, *Chem. Eur. J.* **2006**, *12*, 5878–5884.
[21] P. R. Diamente, R. D. Burke, F. C. J. M. van Veggel, *Langmuir* **2006**, *22*, 1782–1788.
[22] P. R. Diamente, F. C. J. M. van Veggel, *J. Fluoresc.* **2005**, *15*, 543–551.
[23] S. F. Lim, R. Riehn, W. S. Ryu, N. Khanarian, C. K. Tung, D. Tank, R. H. Austin, *Nano Lett.* **2006**, *6*, 169–174.
[24] C. Woghiren, B. Sharma, S. Stein, *Bioconjugate Chem.* **1993**, *4*, 314–318.
[25] H. F. Gaertner, R. E. Offord, *Bioconjugate Chem.* **1996**, *47*, 38–44.
[26] Y. Akiyama, H. Otsuka, Y. Nagasaki, M. Kato, K. Kataoka, *Bioconjugate Chem.* **2000**, *11*, 947–950.
[27] S. Zhang, J. Du, R. Sun, X. Li, D. Yang, S. Zhang, C. Xiong, Y. Peng, *React. Funct. Polym.* **2003**, *56*, 17–25.
[28] F. M. Veronese, *Biomaterials* **2001**, *22*, 405–417.
[29] M. J. Roberts, M. D. Bentley, J. M. Harris, *Adv. Drug Delivery Rev.* **2002**, *54*, 459–476.
[30] H. Otsuka, Y. Nagasaki, K. Kataoka, *Adv. Drug Delivery Rev.* **2003**, *5*, 403–419.
[31] P. Caliceti, M. Chinol, M. Roldo, F. M. Veronese, A. Semenzato, S. Salmaso, G. Paganelli, *J. Controlled Release* **2002**, *83*, 97–108.
[32] R. B. Greenwald, Y. H. Choe, J. McGuire, C. D. Conover, *Adv. Drug Delivery Rev.* **2003**, *55*, 217–250.
[33] T. Ishii, H. Otsuka, K. Kataoka, Y. Nagasaki, *Langmuir* **2004**, *20*, 561–564.
[34] F. Ishii, A. Takamura, H. Ogata, *J. Dispersion Sci. Technol.* **1988**, *9*, 1–15.

Received: February 19, 2010
Published Online: May 14, 2010

Hindawi Publishing Corporation
Journal of Nanomaterials
Volume 2010, Article ID 491471, 7 pages
doi:10.1155/2010/491471

Research Article

Development of Near Infrared-Fluorescent Nanophosphors and Applications for Cancer Diagnosis and Therapy

Tamotsu Zako,[1,2] Hiroshi Hyodo,[3,4,5] Kosuke Tsuji,[3] Kimikazu Tokuzen,[3] Hidehiro Kishimoto,[5,6] Masaaki Ito,[7] Kazuhiro Kaneko,[8] Mizuo Maeda,[1,2] and Kohei Soga[3,4,5]

[1] *Bioengineering Laboratory, RIKEN Institute, 2-1 Hirosawa, Wako, Saitama 351-0198, Japan*
[2] *Nano-Scale Science & Technology Research Group, RIKEN Institute, 2-1 Hirosawa, Wako, Saitama 351-0198, Japan*
[3] *Department of Material Science and Technology, Tokyo University of Science, 2641 Yamazaki, Noda, Chiba 278-8510, Japan*
[4] *Polyscale Technology Research Center, Tokyo University of Science, 2641 Yamazaki, Noda, Chiba 278-8510, Japan*
[5] *Center for Technologies against Cancer, Tokyo University of Science, 2641 Yamazaki, Noda, Chiba 278-8510, Japan*
[6] *Research Institute for Biological Sciences, Tokyo University of Science, 2669 Yamazaki, Noda, Chiba 278-0022, Japan*
[7] *Department of Colorectal and Pelvic Surgery, National Cancer Center Hospital East, Kashiwanoha 6-5-1, Kashiwa, Chiba 277-8577, Japan*
[8] *Division of Digestive Endoscopy and Gastrointestinal Oncology, National Cancer Center Hospital East, Kashiwanoha 6-5-1, Kashiwa, Chiba 277-8577, Japan*

Correspondence should be addressed to Tamotsu Zako, zako@riken.jp and Kohei Soga, mail@ksoga.com

Received 1 November 2009; Revised 25 December 2009; Accepted 5 March 2010

Academic Editor: Huisheng Peng

The use of near infrared (NIR) light for biomedical photonics in the wavelength region between 800 and 2000 nm, which is called "biological window", has received particular attention since water and biological tissues have minimal optical loss due to scattering and absorption as well as autofluorescence in this region. Recent development of InGaAs CCD enables observations in this wavelength region. In the present paper, we report development of Yb and Er-doped yttrium oxide nanoparticles (Y_2O_3:YbEr-NP) which show strong NIR emission under NIR excitation (NIR-NIR emission). We also demonstrate that NIR emission can be observed through swine colon wall. Based on these results, we propose a possible application of Y_2O_3:YbEr-NP for cancer diagnosis and therapy using NIR-NIR imaging system. Our results also suggest potential applications of Y_2O_3:YbEr-NP for noninvasive detection of various diseases.

1. Introduction

Bioimaging technique has received particular attention as an essential tool in the field of biomedical research through the observation of biological phenomena both in vivo and in vitro. The use of near infrared (NIR) light in the wavelength region between 800 and 2000 nm for biomedical photonics attracts great interest because this region is a so-called "biological window", where water and biological tissues have minimal absorbance and autofluorescence. As shown in the loss spectrum of human skin [1] (see Figure 1 of Supplementary Material available online at doi:10.1155/2010/491471.), one can expect the lowest loss of the spectrum within the above region.

Recently, upconverting (UC) phosphors (UCPs) have been used for bioimaging (Figure 1) [2–8]. UCPs are ceramic materials containing rare earth ions. The materials can absorb IR radiation and upconvert it to emit visible light by stepwise excitation among discrete energy levels of the rare earth ions (NIR-VIS imaging) [9]. For example, yttrium oxide (Y_2O_3) matrix containing several atomic % of erbium (Er) exhibits upconversion emission at 550 nm (green) and 660 nm (red) following excitation at 980 nm. The advantage of NIR-VIS bioimaging is that NIR light can penetrate deeper into tissues due its lower scattering.

The wavelength for biomedical photonics has been limited due to the use of the silicon-based CCD. The observation wavelength is limited to at most 1100 nm due to the band

gap of silicon. In recent years, however, the InGaAs CCD which can cover wavelength between 800 and 2200 nm has become available. Considering various advantages of the NIR window, the time is ideal for the development of phosphors to emit fluorescence in this region.

Rare-earth doped ceramics can be a good candidate, since these are known to emit efficient fluorescence in the NIR wavelength region by NIR excitation. For example, the most representative solid state laser material Nd:YAG (Nd-doped yttrium aluminum garnet) can emit light with a wavelength of 1064-nm with 800-nm excitation [10]. Er-doped silicate glass fibers are used to amplify the signal of long-distance fiber optical communication by emitting 1550-nm fluorescence with 980-nm excitation [11]. The authors have previously reported that Er-doped yttrium oxide nanoparticles (Y_2O_3:Er-NP) showed NIR fluorescence (1550 nm) with NIR excitation [12]. The advantage of this NIR-NIR imaging is that both excitation and emission light can penetrate deep into/from tissues, which enables imaging of the target inside the tissues (Figure 1).

In this study, we report a development of Yb and Er-doped yttrium oxide nanoparticles (Y_2O_3:YbEr-NP), which possess higher NIR emission than Y_2O_3:Er-NP. Yb^{3+} was added as a so-called "sensitizer" to increase the NIR emission. Since Yb^{3+} has much larger absorption efficiency and the excitation energy can be efficiently transferred to Er^{3+} in case of upconversion phosphors [9], we added the Yb^{3+} codopant as a sensitizer expecting the same effect for the 1550 nm NIR emission of Er^{3+}. We also demonstrated for the first time that NIR emission could be observed even through the swine colon wall. Based on this observation, we propose possible new NIR-NIR biophotonics applications for cancer diagnosis and therapy using Y_2O_3:YbEr-NP, especially for resection surgery of colon cancer.

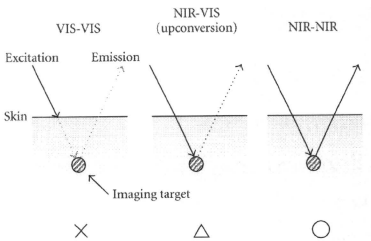

FIGURE 1: Advantage of NIR-NIR imaging system. Near infrared (NIR) emission by NIR excitation is observed using a NIR-NIR system. Due to weaker scattering and absorption, NIR light can penetrate deeper into/from tissues. In contrast, excitation light in the visible (VIS) region cannot reach the imaging target in tissues in the conventional VIS-VIS imaging. In upconversion (NIR-VIS) imaging, although NIR excitation light can reach its target in tissues, only a weak VIS emission can be obtained.

2. Material and Methods

2.1. Materials. $Y(NO_3)_3 \cdot 6H_2O$ (99.99% purity) and Urea (99.0% purity) were purchased from Kanto Chemicals (Tokyo, Japan). $Er(NO_3)_3 \cdot 5H_2O$ (>99% purity), $Yb(NO_3)_3 \cdot 5H_2O$ (99.9% purity) and Na_2CO_3 (99% purity) were obtained from Kojundo Chemical Laboratory (Saitama, Japan).

2.2. Preparation of NIR Biophotonic Nanoparticles. Y_2O_3:YbEr-NP were prepared by the homogeneous precipitation method as used for preparation of upconversion nanoparticles [13]. Twenty mmol/L $Y(NO_3)_3$, 0.2 mmol/L $Yb(NO_3)_3$, and 0.2 mmol/L $Er(NO_3)_3$ were dissolved in 200 mL purified water, mixed with 100 mL of 4 mol/L Urea solution, and stirred for 1 hour at 100°C. The obtained precipitates were separated by centrifugation, and dried at 80°C for 12 hours. The hydroxide or hydroxyl carbonated precursors were calcinated at 1200°C for 60 minutes in an electric furnace to convert them into anhydrous crystalline Y_2O_3 nanoparticles doped with Yb and Er.

2.3. Characterization of NIR Biophotonic Nanoparticles. The prepared Y_2O_3:YbEr-NP were provided for characterization using FE-SEM (S-4200, Hitachi Ltd., Tokyo, Japan) and XRD (XRD-6100, Shimadzu, Kyoto, Japan) with CuKα radiation.

Optical absorption spectra were observed using a spectrometer (U-4000, Hitachi Ltd., Tokyo, Japan) equipped with an integrating sphere. The loss spectrum of the swine colon was also observed using the same equipment and sandwiching a slice of the colon (thickness: 250–330 μm) between two glass slides. The loss spectra were measured in a normal mode without using the integrating sphere.

Fluorescence spectra of Y_2O_3:YbEr-NP and Y_2O_3:Er-NP were recorded using a spectrometer (AvaSpec-NIR256-1.7, Avantes, Eerbeek, Netherlands) under an excitation of 980-nm and a laser diode (LD, SLI-CW-9MM-C1-980-1M-PD, Semiconductor Laser International Corp., USA).

2.4. NIR Imaging System. NIR-NIR imaging was carried out using the NIR imaging system, consisting of a fiber pigtail laser diode at 980 nm with 2 W power (LU0975T050, Lumics, Berlin, Germany), a laser scanner (VM500+, GSI Group, Massachusetts, USA) for planer irradiation of the excitation light, and InGaAs CCD camera (NIR-300PGE, VDS Vosskühler, Osnabrück, Germany) for detection of the NIR fluorescence between 1100 and 1600 nm.

2.5. NIR Imaging Inside Swine Colon. In order to demonstrate that NIR light under NIR excitation can be observed through the colon wall, a tablet of Y_2O_3:YbEr-NP with a diameter of 3 mm and a length of 6 mm was formed by mixing Y_2O_3:YbEr-NP with a conventional dental composite resin (Fuji I, GC, Tokyo, Japan). An endoscopic clip [14] (Olympus, Tokyo, Japan) painted with Y_2O_3:YbEr-NP-containing paint (NIR clip) was also prepared in order to demonstrate that NIR light from the clip can also be observed through colon wall. After fixing the NIR clip in the mucosal side (inside) of a piece of the tubular swine colon, we observed the colon using the NIR-NIR imaging system. It is

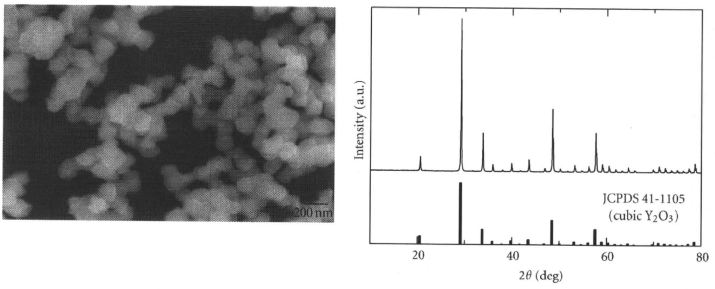

FIGURE 2: Characterization of NIR biophotonic nanoparticles (a) FE-SEM images of Y_2O_3:YbEr-NP synthesized by homogeneous precipitation and calcination at 1200°C for 60 minutes. The particle size was approximately 130 ± 25 nm. The scale bar represents 200 nm. (b) XRD patterns of Y_2O_3:YbEr-NP.

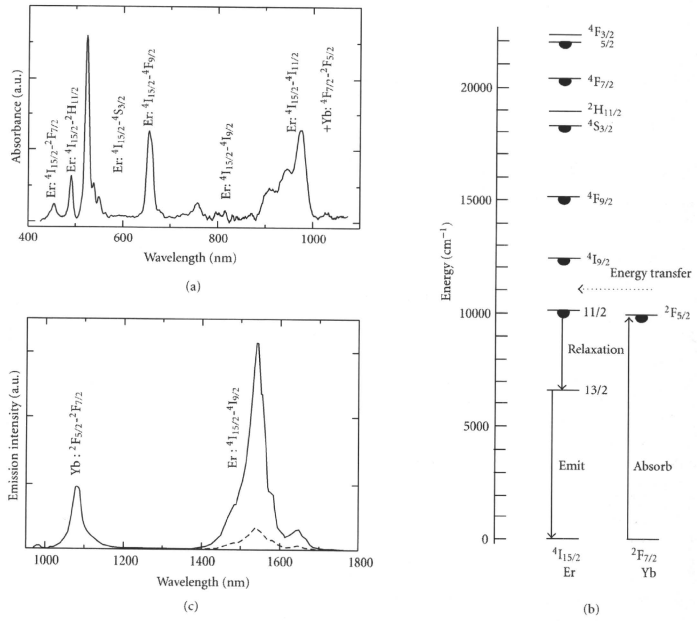

FIGURE 3: (a) Absorption spectrum of Y_2O_3:YbEr-NP. (b) Energy level diagram of Y_2O_3:YbEr-NP. (c) Fluorescence spectra of Y_2O_3:YbEr-NP (solid line) and Y_2O_3:Er-NP (dot line). The fluorescence was measured under an excitation wavelength of 980 nm.

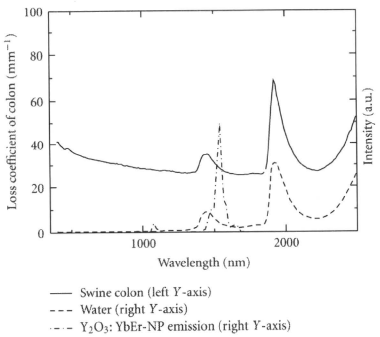

FIGURE 4: Loss spectrum of a sliced sample of swine colon (solid line). The absorption peak at 1420 nm corresponds to the second harmonic of the infrared absorption of water and depends on the water content. The water absorption spectrum is inserted with a dashed line. The emission spectrum of Y_2O_3:YbEr-NP is also incorporated with a chain line.

expected that the painted portion of these endoscopic clips will be observed through the colon wall from the serosal side (outside) of the colon.

3. Results and Discussion

3.1. Characterization of NIR Biophotonic Nanoparticles. Figure 2(a) shows FE-SEM images of Y_2O_3:YbEr-NP synthesized by homogeneous precipitation and calcination at 1200°C for 60 minutes. The particle size was approximately 130 ± 25 nm. Figure 2(b) shows the XRD pattern of Y_2O_3:YbEr-NP. The sample was confirmed to be single-phase Y_2O_3 since all of the peaks were identified as those of cubic Y_2O_3 (JCPDS 41-1105).

3.2. Absorption and Fluorescence Spectra. Absorption and fluorescence spectra of Y_2O_3:YbEr-NP are shown in Figure 3. Yb^{3+} was added as a so-called "sensitizer" for increasing the absorption efficiency of the excitation light at 980 nm in this study. In the absorption spectrum (Figure 3(a)), a strong absorption band of Yb^{3+} was observed. The absorbed excitation light at 980 nm was mainly absorbed by Yb^{3+} and the excitation energy transfers to Er^{3+} to emit the NIR fluorescence at 1550 nm, as shown in Figure 3(b). The absorption and florescence schemes are well known in the field of optical communication and the phenomenon has been well understood [10, 11]. Figure 3(c) shows that the NIR emission of Y_2O_3:YbEr-NP is much higher than that of Y_2O_3:Er-NP, indicating that codoping of Yb^{3+} is also effective to enhance NIR emission.

Figure 4 shows the loss spectrum of the slice of swine colon. The spectrum was obtained by deducting the spectrum due to a thickness of 250 μm from that of 330 μm to yield the net loss due to a swine colon thickness of 110 μm. The spectrum is divided by the corresponding thickness to make it a coefficient spectrum. A water absorption spectrum as well as the emission spectrum of Y_2O_3:YbEr-NP, were also coplotted. There are absorption band peaks at 1420 nm, which are due to the second harmonic absorption of the O-H stretching vibration in water molecules. In the spectrum, the fluorescence spectrum is super imposed. Although the fluorescence and the absorption bands overlap, the tail of the fluorescence is still out of the absorption band and one can expect observation of the fluorescence through the colon wall. It appeared better to select phosphors which could emit fluorescence avoiding the water absorption at 1420 nm. The development of the phosphors that can emit NIR light at different wavelength by doping different rare-earth ions such as Nd, Pr or Tm is now in progress.

3.3. NIR Imaging. Figure 5(a) shows images of the Y_2O_3:YbEr-NP tablet set in a tubular swine colon. The tablet emission could be clearly observed even through the colon wall. This result indicates that the NIR excitation light and the NIR emission from Y_2O_3:YbEr-NP is strong enough to penetrate the colon wall.

In an effort to show the applicability of Y_2O_3:YbEr-NP in cancer therapy, NIR imaging of Y_2O_3:YbEr-NP-coated medical clips and Y_2O_3:YbEr-NP solution injected from the mucosal side (inside) of the colon were carried out. The clips used in this experiment are commercially available for endoscopic therapy and can be easily employed to mark the part of cancer using a conventional endoscopy system. The coating was applied onto the plastic part of the clip. Figure 5(b) shows the NIR imaging Y_2O_3:YbEr-NP-coated clips and those set inside of the swine colon under NIR excitation. Although the coating was as thin as several tens of μm, the NIR fluorescence was clearly observed and was comparable to the case of the tablets.

NIR imaging of Y_2O_3:YbEr-NP solution injected inside the colon was also carried out. As shown in Figure 5(c), NIR emission from Y_2O_3:YbEr-NP injected in the other side of the colon wall was clearly observed. This result suggests that Y_2O_3:YbEr-NP can be used as a substitution for tattoo (black ink) solution which is usually used in cancer therapy as described below. Since tattoo solution is usually injected at both ends of tumor region before laparoscopic surgery, Y_2O_3:YbEr-NP solution was also injected at two points.

3.4. Possible Applications of NIR Photonic Nanomaterials for Cancer Diagnosis and Therapy. The spectroscopic properties of swine colon and the development and demonstrative work using Y_2O_3:YbEr-NP suggest a great potential of NIR-NIR photonic nanomaterials for cancer therapy. For example, this technology can be applied to the intraoperative recognition of the tumor site in laparoscopic surgery for the gastrointestinal cancer (Figures 6(a) and 6(b)). Tattooing

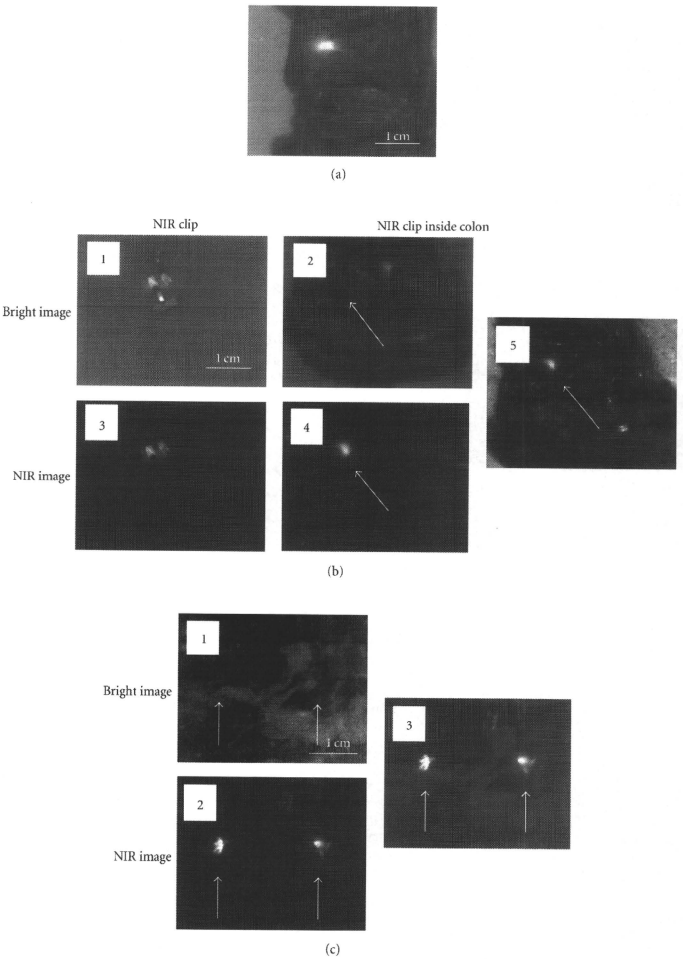

FIGURE 5: NIR imaging (a) Y_2O_3:YbEr-NP tablet set in the tubular sample of swine colon. Hybrid image of bright-field and NIR fluorescence is shown. (b) Bright-filed (1, 2) and NIR fluorescence (3, 4) images of Y_2O_3:YbEr-NP-coated clips (1, 3) and those set inside the swine colon (2, 4). Observations of (2) and (4) are from outside of the colon. Hybrid image of the Y_2O_3:YbEr-NP-coated clips set in the swine colon (5) are shown. Arrows in (2), (4), and (5) show the position of the clip inside swine colon. (c) Y_2O_3:YbEr-NP solution (10 mg/mL) injected from the reverse side of the swine colon. Bright-field (1), NIR fluorescence (2) and hybrid (3) images are shown. Observations are from outside of the colon. Arrows show the injection position of Y_2O_3:YbEr-NP solution inside swine colon.

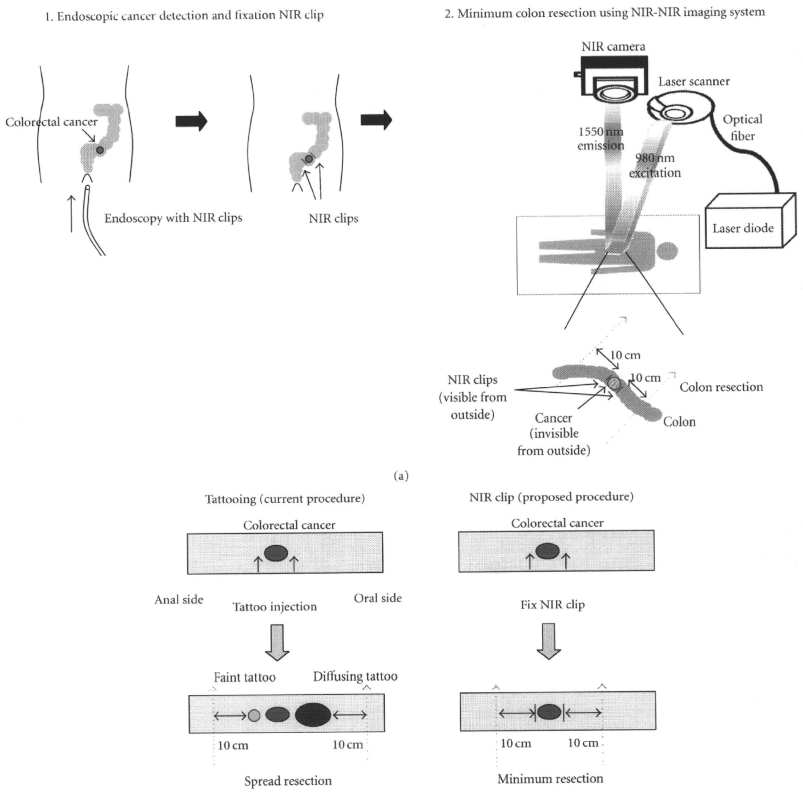

FIGURE 6: Possible application of NIR photonic nanomaterials for cancer therapy. (a) Usage of Y_2O_3:YbEr-NP-coated clips (NIR clips) for colorectal cancer surgery. (1) After endoscopic detection of colorectal cancer, NIR clips are fixed to mark cancer sites using endoscopy. (2) Cancer surgery using NIR-NIR imaging system. Using this new imaging system, we will be able to determine the proper resection margins (normally 10 cm from the cancer site) for curative resection during surgery. (b) Advantage of proposed NIR clip procedure against current procedure (tattooing). NIR clips enable better recognition of cancer sites, which leads to minimum colon resection.

into the submucosal layer of the colon is generally performed in laparoscopic surgery, which sometimes leads to difficulty in recognition of cancer site due to faint tattoo and diffused tattoo, which causes spread resection of the colon (Figure 6(b)) [15]. Figure 6(a) shows our proposed procedure using NIR clips. After endoscopic detection of colorectal cancer, NIR clips are fixed to mark cancer site using endoscopy. Cancer site can be recognized through the serosa of the intestinal wall by NIR fluorescence from the NIR clips fixed inside the colon during cancer surgery using NIR-NIR imaging system. Using this new imaging system, we will be able to determine the proper resection margins (normally 10 cm from the cancer site) for curative resection during surgery, which is much more advantageous compared with the current procedure using tattoo (Figure 6(b)).

Y_2O_3:YbEr-NP can also be used for caner diagnostics. Previously we have demonstrated tumor cell-targeted upconversion imaging using Y_2O_3:Er-NP modified with cyclic

arginine-glycine-aspartic acid (RGD) peptide as a specific probe for tumor cell detection [7]. The RGD peptide strongly binds to integrin $\alpha_v\beta_3$, whose expression is significantly upregulated in invasive tumor cells of certain cancer types (glioblastoma, melanoma, breast, ovarian, and prostate cancers, and in almost all tumor vasculature), but not in quiescent endothelium and normal tissues [16, 17]. Thus, modification of Y_2O_3:YbEr-NP with cyclic RGD peptide will also be useful for the development of a tumor cell-targeted NIR-NIR imaging probe. Successful observation of NIR emission from Y_2O_3:YbEr-NP solution injected inside the colon (Figure 5(c)) supports the idea that targeting and detection of cancer sites in colon using Y_2O_3:YbEr-NP are possible. Research along this line is currently in progress. Our results also suggest that probe-modified Y_2O_3:YbEr-NP could be used for noninvasive detection of various diseases.

Cell toxicity is another important issue when considering probes for use in bioimaging. Previous studies showed that Y_2O_3 and Er^{3+}-doped Y_2O_3 nanoparticles were nontoxic to cultured cell [6, 18]. Since the chemical properties of Yb^{3+} are similar to those of Er^{3+} [19], it is plausible that Yb^{3+} and Er^{3+}-doped Y_2O_3 nanoparticles also are nontoxic. However, further studies on biocompatibility such as inflammation assays and long-term toxicity assays using animal models are important for their medical application.

4. Conclusion

The use of near infrared (NIR) light in the wavelength region between 800 and 2000 nm for biomedical photonics attracts great interest. This region is a so-called "biological window", where water and biological tissues have minimal absorbance and autofluorescence. In the present study, we report high NIR emission under NIR excitation (NIR-NIR emission) of Yb and Er-doped yttrium oxide nanoparticles (Y_2O_3:YbEr-NP), and propose a possible NIR-NIR biophotonic application using Y_2O_3:YbEr-NP for cancer diagnosis and therapy based on demonstrative experiments. Observations of NIR emission through swine colon wall support our idea that NIR-NIR biophotonic nanomaterials can be used for cancer diagnosis and therapy.

Acknowledgments

The authors thank Professor Atsuo Yasumori for the XRD measurement and Dr. Karin Sörgjerd for helpful comments. This work is financially supported by Industrial Technology Research Grant Program from New Energy and Industrial Technology Development Organization (NEDO) of Japan (Tamotsu Zako).

References

[1] R. R. Anderson and J. A. Parrish, "The optics of human skin," *Journal of Investigative Dermatology*, vol. 77, no. 1, pp. 13–19, 1981.

[2] M. Kamimura, D. Miyamoto, Y. Saito, K. Soga, and Y. Nagasaki, "Design of poly(ethylene glycol)/streptavidin coimmobilized upconversion nanophosphors and their application to fluorescence biolabeling," *Langmuir*, vol. 24, no. 16, pp. 8864–8870, 2008.

[3] S. F. Lim, R. Riehn, W. S. Ryu, et al., "In vivo and scanning electron microscopy imaging of upconverting nanophosphors in Caenorhabditis elegans," *Nano Letters*, vol. 6, no. 2, pp. 169–174, 2006.

[4] P. N. Prasad, "Emerging opportunities at the interface of photonics, nanotechnology and biotechnology," *Molecular Crystals and Liquid Crystals*, vol. 415, pp. 1–7, 2004.

[5] S. Sivakumar, P. R. Diamente, and F. C. van Veggel, "Silica-coated Ln^{3+}-Doped LaF_3 nanoparticles as robust down- and upconverting biolabels," *Chemistry: A European Journal*, vol. 12, no. 22, pp. 5878–5884, 2006.

[6] T. Zako, H. Nagata, N. Terada, M. Sakono, K. Soga, and M. Maeda, "Improvement of dispersion stability and characterization of upconversion nanophosphors covalently modified with PEG as a fluorescence bioimaging probe," *Journal of Materials Science*, vol. 43, no. 15, pp. 5325–5330, 2008.

[7] T. Zako, H. Nagata, N. Terada, et al., "Cyclic RGD peptide-labeled upconversion nanophosphors for tumor cell-targeted imaging," *Biochemical and Biophysical Research Communications*, vol. 381, no. 1, pp. 54–58, 2009.

[8] H. J. Zijlmans, J. Bonnet, J. Burton, et al., "Detection of cell and tissue surface antigens using up-converting phosphors: a new reporter technology," *Analytical Biochemistry*, vol. 267, no. 1, pp. 30–36, 1999.

[9] F. Auzel, "Upconversion and anti-stokes processes with f and d ions in solids," *Chemical Reviews*, vol. 104, no. 1, pp. 139–173, 2004.

[10] R. C. Powell, *Physics of Solid State Laser Materials*, Springer, New York, NY, USA, 1998.

[11] S. Sudo, *Optical Fiber Amplifiers: Materials, Devices, and Applications*, Artech House, Norwood, Mass, USA, 1997.

[12] N. Venkatachalam, Y. Okumura, K. Soga, R. Fukuda, and T. Tsuji, "Bioimaging of M1 cells using ceramic nanophosphors: synthesis and toxicity assay of Y_2O_3 nanoparticles," *Journal of Physics: Conference Series*, vol. 191, Article ID 012002, 2009.

[13] N. Venkatachalam, Y. Saito, and K. Soga, "Synthesis of Er^{3+} doped Y_2O_3 nanophosphors," *Journal of the American Ceramic Society*, vol. 92, no. 5, pp. 1006–1010, 2009.

[14] G. S. Raju and L. Gajula, "Endoclips for GI endoscopy," *Gastrointestinal Endoscopy*, vol. 59, no. 2, pp. 267–279, 2004.

[15] K. L. Lane, R. Vallera, K. Washington, and M. R. Gottfried, "Endoscopic tattoo agents in the colon: tissue responses and clinical implications," *American Journal of Surgical Pathology*, vol. 20, no. 10, pp. 1266–1270, 1996.

[16] J. D. Hood and D. A. Cheresh, "Role of integrins in cell invasion and migration," *Nature Reviews Cancer*, vol. 2, no. 2, pp. 91–100, 2002.

[17] H. Jin and J. Varner, "Integrins: roles in cancer development and as treatment targets," *British Journal of Cancer*, vol. 90, no. 3, pp. 561–565, 2004.

[18] D. Schubert, R. Dargusch, J. Raitano, and S.-W. Chan, "Cerium and yttrium oxide nanoparticles are neuroprotective," *Biochemical and Biophysical Research Communications*, vol. 342, no. 1, pp. 86–91, 2006.

[19] K. A. Gschneidner Jr., L. Eyring, and G. H. Lander, *Handbook on the Physics and Chemistry of Rare Earths*, Elsevier, Amsterdam, The Netherlands, 1978.